Available online at www.sciencedirect.com
ScienceDirect
Journal of Sound and Vibration 315 (2008) 664–684
JOURNAL OF SOUND AND VIBRATION
www.elsevier.com/locate/jsvi

Fluid–structure interactions with both structural and fluid nonlinearities

O.O. Bendiksen[a,*], G. Seber[b]

[a]*Mechanical and Aerospace Engineering Department, University of California, Los Angeles, CA 90095-1597, USA*
[b]*Aerospace Engineering Department, Middle East Technical University, Ankara, Turkey*

Accepted 19 March 2008
The peer review of this article was organised by the Guest Editor

Abstract

In this study, we consider a class of nonlinear aeroelastic stability problems, where geometric nonlinearities arising from large deflections and rotations in the structure interact with aerodynamic nonlinearities caused by moving shocks. Examples include transonic panel flutter and flutter of transonic wings of high aspect ratio, where the presence of both structural and aerodynamic nonlinearities can have a dramatic qualitative as well as quantitative effect on the flutter behavior. Both cases represent inherently nonlinear fluid–structure problems, where neglecting either the structural or the fluid nonlinearities can lead to completely erroneous stability predictions. The results presented in this paper illustrate the rich and in some cases surprising flutter behaviors of transonic wings, and the inherent limitations of the von Kármán nonlinear plate model in strongly nonlinear fluid–structure interaction problems of this type.

1. Introduction

Advances in computational methods have made it feasible to study fluid–structure interaction problems where both structural and fluid nonlinearities must be considered in order to capture the correct stability behavior. Previous studies have focused on either structural nonlinearities, especially geometric nonlinearities arising from large deflections [1–5], or fluid nonlinearities arising from shock motion in transonic flows [6–9]. Fluid–structure interaction problems involving both structural and fluid nonlinearities are only recently being investigated [10], and the results are less well understood.

Many of the emerging problems in aeroelasticity involve very flexible wing structures; for example, highly optimized unmanned aerial vehicles (UAVs) and high altitude long endurance (HALE)-type aircraft. Although linear elastic behavior may still be assumed in many of these cases, geometric nonlinearities arising from large deflections and rotations can no longer be ignored, and linear structural codes cannot be expected to predict the correct static or dynamic stability behaviors. The Helios aircraft built by AeroVironment and operated by NASA is a good example of this category, where wing tip deflections during steady flight in the

*Corresponding author. Tel.: +1 310 206 5453; fax: +1 310 206 4830.
E-mail addresses: oddvar@seas.ucla.edu (O.O. Bendiksen), gseber@hotmail.com (G. Seber).

0022-460X/$ - see front matter © 2008 Published by Elsevier Ltd.
doi:10.1016/j.jsv.2008.03.034

Nomenclature

A	wing aspect ratio
A_i	triangular area coordinates
c	wing or panel chord
D	$Eh^3/12(1-\nu^2)$ = plate flexural rigidity
e	total energy (fluid)
E	Young's modulus
E_{tot}	total energy (structure) = $T+U$
G	shear modulus
h	plate thickness
k	$\omega c/2U_\infty$ = reduced frequency; also shear correction factor
M	Mach number
$\mathbf{n}$	rotation vector
$\mathbf{n}_d$	deformed nodal vector
p	pressure
q	$\rho_\infty U_\infty^2/2$ = dynamic pressure
$\mathbf{q}$	generalized coordinate vector
t	time
T	kinetic energy
$\mathbf{u}$	fluid velocity vector with components u_i
$\mathbf{U}$	mesh velocity vector with components U_i
u,v,w	plate displacements in the x, y, z directions
U	strain energy
U_∞	freestream velocity at upstream infinity
α	angle of attack
β_x, β_y	rotations of normals in the x–z and y–z planes, respectively
γ	ratio of specific heats
$\{\gamma\}$	shear strains
$\{\varepsilon_m\}$	membrane strains
$\{\varepsilon_n\}$	nonlinear strains
$\{\kappa\}$	plate element curvatures
λ	taper ratio
Λ	sweep angle
ν	Poisson's ratio
ρ	air density
ρ_m	plate mass density
τ	nondimensional time = $\omega_{1T}t/2\pi$
ω	circular frequency
ω_{1T}	frequency of first torsion mode in vacuum

Superscripts and subscripts

r, LE, TE	wing root, leading, and trailing edge, respectively
∞	conditions at upstream infinity

range of 10–20 ft were observed, with dynamic excursions beyond 20 ft. The aircraft was destroyed in a flight mishap in June of 2003. The instability that caused the structural breakup of the aircraft appears to have involved nonlinear aero-structural–controls interactions.

The von Kármán nonlinear plate model has been used in a number of previous nonlinear flutter studies, including supersonic panel flutter [1,2], transonic panel flutter [11,12], and limit cycle oscillation (LCO)-type flutter studies of low-aspect-ratio wings [4,5,13]. Recent results, however, indicate that this nonlinear strain–displacement model is not suitable for incorporation into a general-purpose aeroelastic code, because of its relatively limited range of validity and high sensitivity to the in-plane boundary conditions [5,10]. This is especially true for cantilever swept wings, where the von Kármán model overestimates the stiffening effect from the in-plane strains, leading to an underestimation of the LCO amplitudes. This excess stiffness is clearly evident in the comparisons between theory and experiments of LCO amplitudes of the flat plate delta wings studied in Refs. [5,13].

The objective of this paper is to show that geometrically nonlinear aeroelastic problems with strong fluid nonlinearities arising from shock motion are inherently nonlinear, in the sense that neglecting either the structural or the fluid nonlinearities can lead to completely erroneous stability predictions. As a result, these problems can exhibit a pronounced sensitivity to the accuracy and fidelity of the structural model. Not surprisingly, this sensitivity is problem dependent. In the case of transonic flutter of thin plates, for example, the von Kármán model appears to yield results that are qualitatively and quantitatively correct, within the expected engineering accuracy, at least for cases where none of the edges are free. But in the case of a cantilever swept wing of high aspect ratio, the von Kármán model is not applicable, because tip deflections of the order of the wing chord must be considered. Furthermore, because of the presence of shocks on the wing surface, there is a strong interaction between the structural nonlinearities arising from large deflections and aerodynamic nonlinearities arising from shock motion. In the swept wing case, the so-called structural

washout effect plays an important role, and also interacts with the aerodynamic nonlinearities. As the wing bends, it unloads the outboard region, reducing the shock strengths and moving the shocks forward, towards the leading edge. The weaker and more forward shocks lead to an earlier transition (at lower amplitudes) from Type A (continuous) to Type B (intermittent) shock motion, resulting in a limit cycle flutter mode that persists over a relatively wide range of dynamic pressures and flight altitudes.

In the case of panel flutter, interactions between the structural and aerodynamic nonlinearities in the strongly nonlinear transonic range, $0.95 \leqslant M \leqslant 1.2$, lead to travelling wave flutter, in the generalized sense, and the panel motions at different chord locations are significantly out of phase. It is interesting to note that the prevailing flutter mode is a travelling wave even in panels of low chord-to-width ratios, where earlier studies based on linearized aerodynamics predict single-degree-of-freedom flutter [14–16]. Inclusion of structural nonlinearities using a von Kármán plate model does not change this conclusion; see Fig. 1 of Ref. [1], which indicates that travelling wave flutter is not predicted by linearized aerodynamic theories, except for plates of very large chord-to-width ratio. Only when both structural and aerodynamic nonlinearities are modeled do we obtain travelling wave flutter in the high-aspect-ratio case [12]. As the Mach number is decreased from the supersonic and into the transonic region, the flutter mode changes from a standing wave to a travelling wave. The presence of oscillating shock waves on the panel surface plays a significant role in this flutter mode change. Travelling wave flutter was indeed observed in some of the early panel flutter tests [17,18]. In experiments involving buckled panels, travelling wave flutter in the generalized sense has been observed at supersonic Mach numbers as well [19,20].

2. Computational approach

Two different finite element models of the geometric nonlinearities are considered. The first is the von Kármán nonlinear plate model, which has been used in several previous studies of panel and wing flutter [1,2,4,11–13]. This model is based on Kirchhoff–Love plate theory and is only used in calculating the transonic panel flutter results in the present paper.

The second computational model is based on a nonlinear finite element formulation of the fluid–structure system, Fig. 1, using individual element-fixed local Lagrangian coordinate systems, Fig. 2, to account for the geometric nonlinearities arising from large displacements and rotations [10]. The approach is a generalization of the Direct Eulerian–Lagrangian computational scheme [9], implemented using a Galerkin finite element discretization of the Euler equations in the fluid domain and Mindlin–Reissner finite elements in the structural domain. Finite rotation relations are used to update the nodal displacement vector at each stage in the Runge–Kutta time-stepping scheme.

In both computational schemes, the calculations are done at the element level in the fluid and structural domains, and the fluid–structure system is time-marched as a single dynamical system. The exact nonlinear fluid–structure boundary condition is satisfied using the actual deformation of the structure, as defined by the finite element shape functions and the local element coordinates. To ensure strict synchronization between the fluid and structural domains, the unsteady fluid pressures at the structural surface are calculated in a time-accurate manner by solving the two-dimensional (2D) or three-dimensional (3D) Euler equations, within the same multistage Runge–Kutta loop.

3. Nonlinear structural models

3.1. Von Kármán finite element plate model

The panel is modeled using 2D plate elements to represent a thin, isotropic plate undergoing cylindrical bending. The cylindrical bending assumption approximates a plate of large width-to-chord ratio, and neglects variations of lateral plate displacements in the spanwise (y) direction. As is customary, the middle surface (MS) of the undeflected plate is in the x,y plane, and the flow is in the positive x-direction; see Fig. 3. Both pinned and clamped boundary conditions at the leading and trailing edges ($x = 0,\ c$) have been implemented. The axial displacements at the supports are assumed zero. The latter assumption introduces a

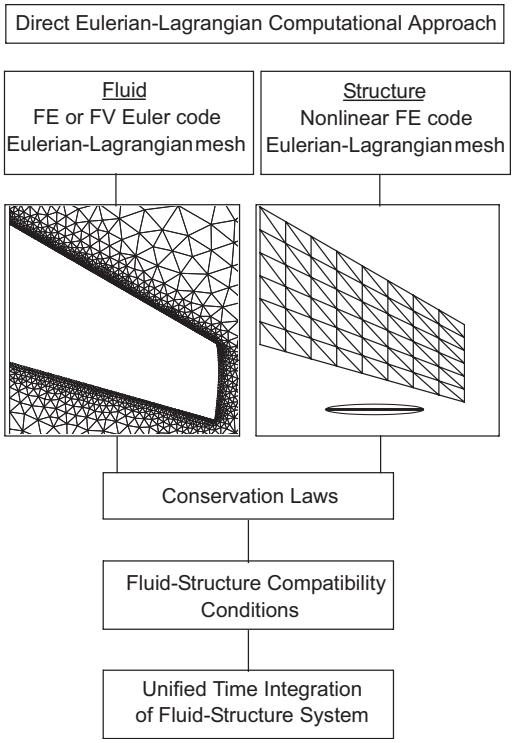

Fig. 1. The direct Eulerian–Lagrangian computational approach.

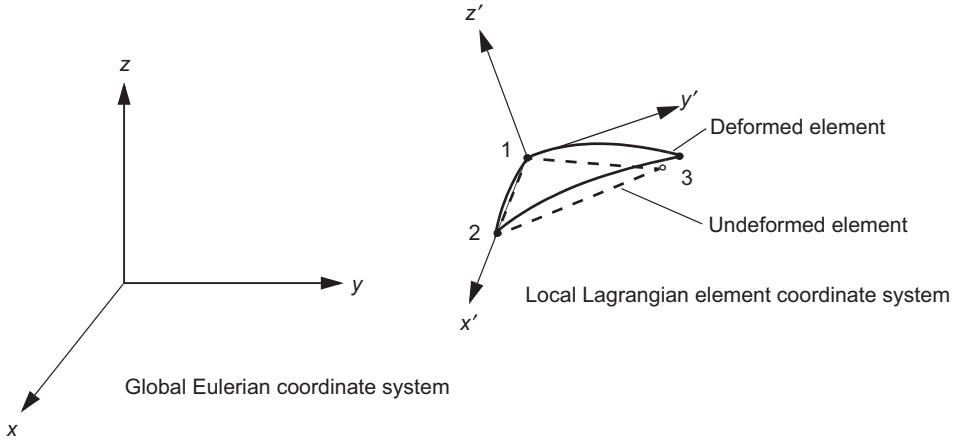

Fig. 2. Eulerian and Lagrangian coordinate systems used in the direct Eulerian–Lagrangian computational scheme.

nonlinear term in the structural equations, resulting from the in-plane stretching of the MS of the plate as it deforms.

The finite element matrices are based on the von Kármán plate equations, which in the 2D case can be reduced to the following single equation for the lateral deflection of the plate:

$$D\frac{\partial^4 w}{\partial x^4} - (N_x + N_{x0})\frac{\partial^2 w}{\partial x^2} + \rho_m h\frac{\partial^2 w}{\partial t^2} = p_\infty - p \tag{1}$$

Cavity effects are ignored, i.e., the pressure in the cavity below the plate is assumed constant and equal to p_∞. Here, N_{x0} is the in-plane loading due to external forces, and N_x is the additional in-plane force induced by

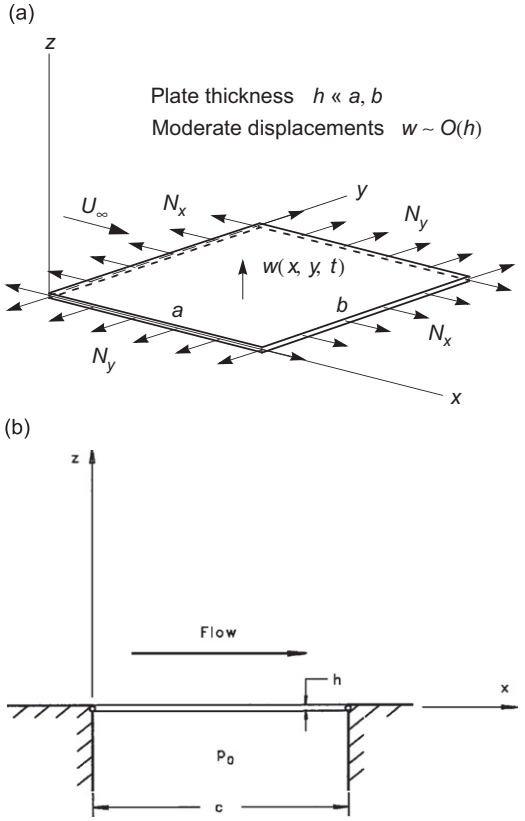

Fig. 3. (a) Panel geometry and coordinate system, (b) two-dimensional idealization for a panel of high aspect ratio.

the deflection w:

$$N_x = \frac{Eh}{2c}\int_0^c \left(\frac{\partial w}{\partial x}\right)^2 \mathrm{d}x \tag{2}$$

Eq. (1) is discretized using standard finite element techniques, resulting in a set of matrix equations of the form

$$\frac{\mathrm{d}}{\mathrm{d}t}\mathbf{m}_i\dot{\mathbf{q}}_i + \mathbf{Q}_i^E - \mathbf{Q}_i^F = \mathbf{0} \tag{3}$$

for a typical (ith) element, with generalized coordinates

$$\mathbf{q}_i = \begin{bmatrix} w_i \\ \theta_i \\ w_{i+1} \\ \theta_{i+1} \end{bmatrix} \tag{4}$$

where w_i and θ_i represent the lateral (bending) displacement and rotation at the left (ith) node of the element, respectively. A lumped mass matrix is used, given by

$$\mathbf{m} = \rho_m hL \begin{bmatrix} 1/2 & 0 & 0 & 0 \\ 0 & L^2/24 & 0 & 0 \\ 0 & 0 & 1/2 & 0 \\ 0 & 0 & 0 & L^2/24 \end{bmatrix} \tag{5}$$

for an element of length L. The generalized fluid forces $\mathbf{Q}_i^F$ on each element are evaluated by solving the unsteady Euler equations, simultaneously with the structural equations. The generalized elastic forces in the ith element can be expressed as a sum of two terms:

$$\mathbf{Q}_i^E = (\mathbf{k} + \mathbf{k}_g)_i \mathbf{q}_i \tag{6}$$

where $\mathbf{k}$ is the linear part of the stiffness matrix and $\mathbf{k}_g$ is the geometric stiffness matrix arising from the in-plane stretching caused by lateral deflections of the plate. The linear stiffness matrix for the element is of the form

$$\mathbf{k} = \frac{D}{L^3}\begin{bmatrix} 12 & 6L & -12 & 6L \\ 6L & 4L^2 & -6L & 2L^2 \\ -12L & -6L & 12 & -6L \\ 6L & 2L^2 & -6L & 4L^2 \end{bmatrix} \tag{7}$$

The nonlinear (geometric) stiffness matrix can be expressed in the form

$$\mathbf{k}_g = (N_{x0} + N_x) k_{g0} \tag{8}$$

where

$$\mathbf{k}_{g0} = \frac{1}{30L}\begin{bmatrix} 36 & 3L & -36 & 3L \\ 3L & 4L^2 & -3L & -L^2 \\ -36 & -3L & 36 & -3L \\ 3L & -L^2 & -3L & 4L^2 \end{bmatrix} \tag{9}$$

It follows from Eq. (8) that $\mathbf{k}_g$ is proportional to $(N_x + N_{x0})$ and thus depends on the deformations of all elements of the panel, as is obvious from Eq. (2). For a panel of n elements, the in-plane tension caused by lateral deflections becomes

$$N_x = \frac{Eh}{2c}\sum_{i=1}^{n} \mathbf{q}_i^{\mathrm{T}} \mathbf{k}_{g0_i} \mathbf{q}_i \tag{10}$$

The structural equations of motion for the entire panel are of the same generic form as Eq. (3), with the matrices now representing assembled mass and stiffness matrices. We do not, however, perform such an assembly; instead, the entire aeroelastic system of space-discretized finite element equations is integrated simultaneously, as outlined in Ref. [9]. In this procedure, only local assembly at individual nodes is performed, and the fluid and solid elements are treated in a parallel manner. The subscript i in Eq. (3) now refers to the ith node rather than the ith element, and the equations are time-marched node by node, both in the structural and fluid domains. Further details of the implementation of the direct integration scheme as applied to the panel flutter problem can be found in Refs. [11,12].

3.2. Mindlin–Reissner finite element in a mixed Eulerian–Lagrangian formulation

Fig. 2 shows a typical triangular structural finite element and the associated coordinate systems. The xyz system is a fixed (or inertial) Eulerian system with respect to which the response of the wing structure is expressed. The $x'y'z'$ system is an element-fixed (moving) local coordinate system, and is Lagrangian in the sense that the axes are fixed to three points in the element. The elastic deformations in each element are calculated relative to these local systems; hence, the overall formulation may be considered "mixed" Eulerian–Lagrangian.

At any given time step, the three nodes of the triangle form a plane in the global coordinate system. The z'-axis is defined orthogonal to this plane by taking the cross-product of the two planar vectors from the origin (node 1) to the remaining two nodes. The x'-axis is aligned along nodes 1 and 2, and the y'-axis orientation is chosen such that a right-handed coordinate system results. Note that this choice of the local coordinate system automatically eliminates the local out-of-plane displacements at each node, i.e., $w'_1 = w'_2 = w'_3 = 0$.

During time-marching of the fluid–structure system, generalized coordinates and forces are expressed in both the local element coordinates and the global system coordinates, as required. For example, if $\mathbf{q}^L$ and $\mathbf{q}^G$ are identical vectors expressed in the local and global coordinate systems, respectively, they are related through the orthogonal transformation

$$\mathbf{q}^L = \mathbf{e}\mathbf{q}^G \tag{11}$$

$$\mathbf{e} = \begin{bmatrix} (e_{x'})_1 & (e_{x'})_2 & (e_{x'})_3 \\ (e_{y'})_1 & (e_{y'})_2 & (e_{y'})_3 \\ (e_{z'})_1 & (e_{z'})_2 & (e_{z'})_3 \end{bmatrix} \tag{12}$$

where $(e_{x'})_i$, $(e_{y'})_i$, $(e_{z'})_i$ $(i = 1,2,3)$ are the components of the local coordinate system unit vectors expressed in the global coordinate system, i.e., the direction cosines between the corresponding coordinate axes.

The nonlinear finite element is constructed as shown in Fig. 4. A discrete shear triangle (DST) is used to model the out-of-plane bending and the transverse shear behavior, based on the formulations in Refs. [21,22]. The in-plane motion of the element is modeled using a constant strain triangle (CST), and the associated shape functions are used in connection with the corresponding shape functions of the DST to create the stress-stiffening matrix in local element coordinates. Because the deformations relative to the local Lagrangian element coordinate system are of the order of the element thickness or less, the von Kármán theory can be used to formulate this geometric stiffness matrix. It must be emphasized that the mixed formulation is essential here for the validity of this step. If one attempts to express the geometric stiffness matrix in terms of the displacements relative to the inertial system x,y,z, the formulation reverts back to a classical von Kármán model, which cannot cope with the large displacements and rotations encountered in aeroelastic problems of flexible wings of high aspect ratio. In fact, recent computational experience indicates that the von Kármán theory gives poor or misleading results even for wings of low aspect ratio, e.g., the delta wing studied in Ref. [5].

The total strain energy of an element can be expressed as a sum of the component strain energies as

$$U^e_{\text{total}} = U_m + U_b + U_s + U_{N1} + U_{N2} \tag{13}$$

$$U_m = \frac{1}{2}\int_{A_e} \{\varepsilon_m\}^{\mathrm{T}}[D_m]\{\varepsilon_m\}\mathrm{d}A$$

$$U_b = \frac{1}{2}\int_{A_e} \{\kappa\}^{\mathrm{T}}[D_b]\{\kappa\}\mathrm{d}A$$

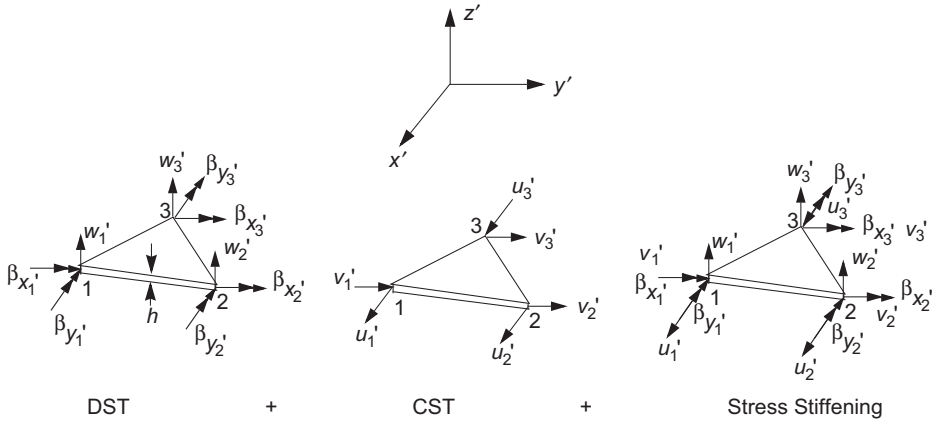

Fig. 4. Components of the nonlinear Mindlin–Reissner plate finite element.

$$U_s = \frac{1}{2}\int_{A_e} \{\gamma\}^{\mathrm{T}}[D_s]\{\gamma\}\mathrm{d}A$$
$$U_{N1} = \int_{A_e} \{\varepsilon_m\}^{\mathrm{T}}[D_m]\{\varepsilon_n\}\mathrm{d}A$$
$$U_{N2} = \int_{A_e} \{\varepsilon_n\}^{\mathrm{T}}[D_m]\{\varepsilon_n\}\mathrm{d}A \tag{14}$$

where A_e is the element area and

$$[D] = \frac{E}{1-v^2}\begin{bmatrix} 1 & v & 0 \\ v & 1 & 0 \\ 0 & 0 & \dfrac{1-v}{2} \end{bmatrix} \tag{15}$$

$$[D_m] = h[D]; \quad [D_b] = \frac{h^3}{12}[D] \tag{16}$$

$$[D_s] = kGh\begin{bmatrix} 1 & 0 \\ 0 & 1 \end{bmatrix} = \frac{kEh}{2(1+v)}\begin{bmatrix} 1 & 0 \\ 0 & 1 \end{bmatrix} \tag{17}$$

Here, k is the shear correction factor (= 5/6 for isotropic plates). In equations (14), U_m, U_b, and U_s are the quadratic-order strain energies representing the membrane stretching (CST), out-of-plane bending and shear (DST), respectively. The cubic-order strain energy U_{N1} represents the nonlinear coupling of the in-plane and out-of-plane motion, and the quartic-order strain energy U_{N2} represents the nonlinear coupling effect of slope due to large deflections. The strains and curvatures are related to the element displacements, as follows:

$$\{\varepsilon_m\}^{\mathrm{T}} = \left\{\frac{\partial u_0'}{\partial x'} \quad \frac{\partial v_0'}{\partial y'} \quad \frac{\partial v_0'}{\partial x'} + \frac{\partial u_0'}{\partial y'}\right\}$$
$$\{\kappa\}^{\mathrm{T}} = \left\{\frac{\partial \beta_{x'}}{\partial x'} \quad \frac{\partial \beta_{y'}}{\partial y'} \quad \frac{\partial \beta_{y'}}{\partial x'} + \frac{\partial \beta_{x'}}{\partial y'}\right\}$$
$$\{\gamma\}^{\mathrm{T}} = \left\{\frac{\partial w_0'}{\partial x'} + \beta_{x'} \quad \frac{\partial w_0'}{\partial y'} + \beta_{y'}\right\}$$
$$\{\varepsilon_n\}^{\mathrm{T}} = \left\{\frac{1}{2}\beta_{x'}^2 \quad \frac{1}{2}\beta_{x'}^2 \quad \beta_{x'}\beta_y\right\} \tag{18}$$

where

$$u'(x', y', z', t) = u_0'(x', y', t) + z'\beta_{x'}(x', y', t)$$
$$v'(x', y', z', t) = v_0'(x', y', t) + z'\beta_{y'}(x', y', t)$$
$$w'(x', y', t) = w_0'(x', y', t) \tag{19}$$

and u_0', v_0', and w_0' are the corresponding displacements of the plate MS.

In order to obtain an element free of shear locking, the equilibrium equations are used to solve for the transverse shear strains $\{\gamma\}$, with the help of the constitutive equations. The element stiffness matrix is then formulated using quadratic interpolation functions for the rotation fields

$$\beta_x = \sum_{i=1}^{6} N_i(\xi, \eta)\beta_{x_i}(t); \quad \sum_{i=1}^{6} N_i(\xi, \eta)\beta_{y_i}(t) \tag{20}$$

where β_{x_i} and β_{y_i} are the nodal values at the corner nodes 1,2,3 and the mid-side nodes 4,5,6, and primes have been dropped for convenience. After eliminating $w_{,x}$ and $w_{,y}$ at the corner nodes and β_n and β_s at the mid-side nodes, the number of unknowns associated with the flexural and transverse shear problem is reduced to nine,

$$\{q_{w\beta}^e\} = \{w_1\ \beta_{x_1}\ \beta_{y_1}\ w_2\ \beta_{x_2}\ \beta_{y_2}\ w_3\ \beta_{x_3}\ \beta_{y_3}\}^{\mathrm{T}} \tag{21}$$

The stiffness matrix for the in-plane CST element is based on linear interpolation functions, and the development is well-known and available in standard finite element texts. The final displacement vector for the "assembled" triangle used in the present study is given by

$$\{q^e\} = \{w_1\ \beta_{x_1}\ \beta_{y_1}\ w_2\ \beta_{x_2}\ \beta_{y_2}\ w_3\ \beta_{x_3}\ \beta_{y_3} \quad u_1\ v_1\ u_2\ v_2\ u_3\ v_3\}^{\mathrm{T}} \tag{22}$$

The 15×15 element stiffness matrix of the nonlinear model can be obtained from the principle of stationary potential energy, using the strain energy relations (14). To calculate the nonlinear coupling partition, the values of the nodal degrees of freedom are required at the current time step. The structure of the element stiffness matrix is as follows:

$$[K_e]_{15\times 15} = \begin{bmatrix} [\mathrm{DST}] & [\mathrm{NLC}] \\ [\mathrm{NLC}]^{\mathrm{T}} & [\mathrm{CST}] \end{bmatrix} \tag{23}$$

where $[\mathrm{DST}]_{9\times 9}$ is the out-of-plane partition, $[\mathrm{CST}]_{6\times 6}$ the in-plane partition, and $[\mathrm{NLC}]_{9\times 6}$ the nonlinear coupling partition.

The element in-plane deformations are calculated by comparing the deformed element to its undeformed state, to determine the nodal displacements. Similarly, the element flexural deformations arising from the nodal rotations $\beta_{x'}$, $\beta_{y'}$ are determined by comparing the deformed and undeformed unit vectors at the element nodes. The undeformed nodal vectors are normal to the plane formed by the triangle nodes at all times, and coincide with the local z'-axis. The deformed unit vectors are updated at each time step by the incremental rotations in the global x and y directions, using the finite rotation relation

$$\mathbf{n}_d^{t^{n+1}} = \cos(\Delta\phi)\mathbf{n}_d^{t^n} + (1-\cos(\Delta\phi))(\mathbf{n}\cdot\mathbf{n}_d^{t^n})\mathbf{n} + \sin(\Delta\phi)(\mathbf{n}\times\mathbf{n}_d^{t^n}) \tag{24}$$

where

$$\Delta\phi = \sqrt{(\Delta\beta_x)^2 + (\Delta\beta_y)^2 + (\Delta\beta_z)^2} \tag{25}$$

is the magnitude of the rotation, and

$$\mathbf{n} = (-\Delta\beta_y\mathbf{i} + \Delta\beta_x\mathbf{j} + \Delta\beta_z\mathbf{k})/\Delta\phi \tag{26}$$

is the normalized rotation vector, and $\mathbf{n}_d^{t^n}, \mathbf{n}_d^{t^{n+1}}$ are the deformed unit vectors at time steps n and $n+1$, respectively, expressed in the global coordinate system.

Although the incremental rotations at each step can be approximated as infinitesimal rotations, the use of finite rotation expressions has been found to provide more accurate solutions, with a minimal increase in computational cost. By determining the amount of rotation that the undeformed vector must undergo to coincide with the corresponding deformed vector, local rotational deformations can be calculated in terms of the deformed unit vector expressed in local coordinates, i.e., $(\mathbf{n}_d^{t^n})^L$, at the beginning of each time step t^n, as follows:

$$\beta_{x'} = (\mathbf{n}_d^{t^n})_x^L \frac{\cos^{-1}((\mathbf{n}_d^{t^n})_z^L)}{\sqrt{((\mathbf{n}_d^{t^n})_x^L)^2 + ((\mathbf{n}_d^{t^n})_y^L)^2}}, \quad \beta_{y'} = (\mathbf{n}_d^{t^n})_y^L \frac{\cos^{-1}((\mathbf{n}_d^{t^n})_z^L)}{\sqrt{((\mathbf{n}_d^{t^n})_x^L)^2 + ((\mathbf{n}_d^{t^n})_y^L)^2}} \tag{27}$$

Cubic interpolation functions are used as a basis for deriving the consistent mass matrix and the generalized aerodynamic loads associated with the out-of-plane degrees of freedom. For the in-plane degrees of freedom, we make use of the standard mass matrix for the CST element, and the corresponding generalized aerodynamic forces are calculated using the associated linear shape functions for the element. All integrals are evaluated using Gaussian integration in natural (triangular) coordinates. Because the Gaussian integration points are fixed with respect to the fluid elements at the wing surface, this procedure leads to an efficient and accurate numerical evaluation of the consistent generalized aerodynamic forces.

4. Nonlinear fluid model

In the present computational approach, it is convenient to base the fluid dynamics model on the integral or weak form of the conservation laws,

$$\frac{\partial}{\partial t}\int_{\Omega}\mathbf{W}dV+\int_{\partial\Omega}\mathbf{F}\cdot\mathbf{n}\,\mathrm{d}S=0 \tag{28}$$

where Ω is an element volume with boundary $\partial\Omega$ moving with velocity $\mathbf{U}$, $\mathbf{n}=n_i\mathbf{e}_i$ is the outward unit normal to $\partial\Omega$, $\mathbf{e_i}$ are the unit vectors in the x_i directions, and

$$\mathbf{W}=\begin{bmatrix}\rho\\ \rho u_1\\ \rho u_2\\ \rho u_3\\ \rho e\end{bmatrix}$$
$$\mathbf{F}_j=\begin{bmatrix}\rho(u_j-U_j)\\ \rho u_1(u_j-U_j)-\sigma_{1j}\\ \rho u_2(u_j-U_j)-\sigma_{2j}\\ \rho u_3(u_j-U_j)-\sigma_{3j}\\ \rho e(u_j-U_j)-\sigma_{ij}u_i\end{bmatrix} \tag{29}$$

Here, ρ is the density, $\mathbf{u}$ the material velocity, and e the total energy per unit mass. Furthermore, u_j and U_j are the Cartesian components of $\mathbf{u}$ and $\mathbf{U}$, respectively, σ_{ij} is the cartesian stress tensor, and $\mathbf{F}=\mathbf{F}_j\mathbf{e}_j$. In the inviscid (Euler) flow model used in this paper, $\sigma_{ij}=-p\delta_{ij}$, and the equation of state is used to eliminate the pressure p.

By using a mixed Eulerian–Lagrangian formulation, a Galerkin finite element discretization can be obtained on an unstructured mesh, including the effects of mesh motion and element deformations. A typical Galerkin finite element discretization results in a space-discretized set of nodal equations for the fluid domain of the form [9]

$$\frac{\mathrm{d}}{\mathrm{d}t}\left(\sum_j\mathbf{m}_{ij}\mathbf{W}_j\right)+\mathbf{Q}_i-\mathbf{D}_i=0 \tag{30}$$

where $\mathbf{W}_j$ are the nodal values of $\mathbf{W}$, and the summation on j extends over all nodes in the "superelement" or control volume associated with node i, i.e., the union of all elements that meet at node i. Here, $\mathbf{m}_{ij}$ is the consistent mass matrix, $\mathbf{Q}_i$ is the flux vector, and $\mathbf{D}_i$ is a vector of dissipative fluxes of a suitable type, to capture shocks and stabilize the scheme. For example, the Jameson–Mavriplis-type dissipation operators have been found to be very well suited for nonlinear aeroelastic calculations. For further details, see Ref. [9].

A finite element discretization of the structural domain (wing structure) leads to a similar set of equations, in term of the generalized Lagrangian displacement coordinates $\mathbf{q}_j$ at the nodes:

$$\frac{\mathrm{d}}{\mathrm{d}t}\left(\sum_j\mathbf{m}_{ij}\dot{\mathbf{q}}_j\right)+\mathbf{Q}_i^E+\mathbf{Q}_i^D-\mathbf{Q}_i^F=0 \tag{31}$$

where the sum (assembly) must be carried out over all elements that meet at node i. Here, $\mathbf{Q}_i{}^E$ are the elastic forces, $\mathbf{Q}_i{}^D$ are the structural damping forces, and $\mathbf{Q}_i{}^F$ are the consistent generalized fluid forces associated with the ith node.

A multistage Runge–Kutta scheme is used to integrate the space-discretized system of nonlinear equations forward in time. Time accuracy is maintained by ensuring that the fluid and structural finite element equations are time-marched simultaneously, within the same multistage Runge–Kutta execution loop. The numerical calculations start with the converged steady aeroelastic (or the steady aerodynamic) solution for the wing.

A suitable initial velocity is then imparted to the model in bending or in torsion (or both), and the time-marching solution is initiated.

5. Fluid–structure coupling

The fluid–structure boundary condition of tangent flow is satisfied on the exact fluid–structure boundary, using the actual deformations and velocities of the wing surface, as defined by the finite element shape functions and the generalized coordinates and velocities at the current time step. Although this type of implementation is more difficult than a loosely coupled scheme that lacks strict synchronization, it is essential for obtaining the correct energy exchange between the fluid and the structure.

In the direct Eulerian–Lagrangian finite element code, the consistent unsteady fluid forces are first calculated in the local element coordinate systems, using 13-point Gaussian quadrature, and then transformed to the global system as the space-discretized aeroelastic equations are time-marched. The resulting unsteady fluid forces are captured as true *follower forces*, resulting in a more accurate prediction of the dynamic response and stability of the wing.

6. Results

Results are presented for two aeroelastic stability problems where structural and fluid nonlinearities play a fundamental role: (1) transonic panel flutter and (2) transonic flutter of a high-aspect-ratio swept wing.

6.1. Transonic panel flutter

Fig. 5 shows the unstructured triangular mesh used in the fluid domain, with a total of 1804 nodes, of which 51 nodes were on the panel surface. The far-field boundary was set at a radius of 25 panel chords, Fig. 5b. The plate structure was discretized using 10 structural finite elements, although select calculations with 25 elements have also been performed to check convergence. In all results presented here, the externally applied in-plane load N_{x0} was set to zero, but the in-plane stretch term N_x was retained in the equations.

In the strongly nonlinear transonic range, at or near Mach 1, interactions between the structural and aerodynamic nonlinearities lead to travelling wave flutter. Fig. 6 shows this type of flutter for a thin ($h/c = 0.004$), simply supported aluminum panel at 20,000 ft altitude. Part (a) of the figure shows the transverse displacements at 1/4-chord, midchord, and 3/4-chord, as a function of time. Significant phase differences are observed between the chord locations, indicating that the flutter mode is a generalized wave

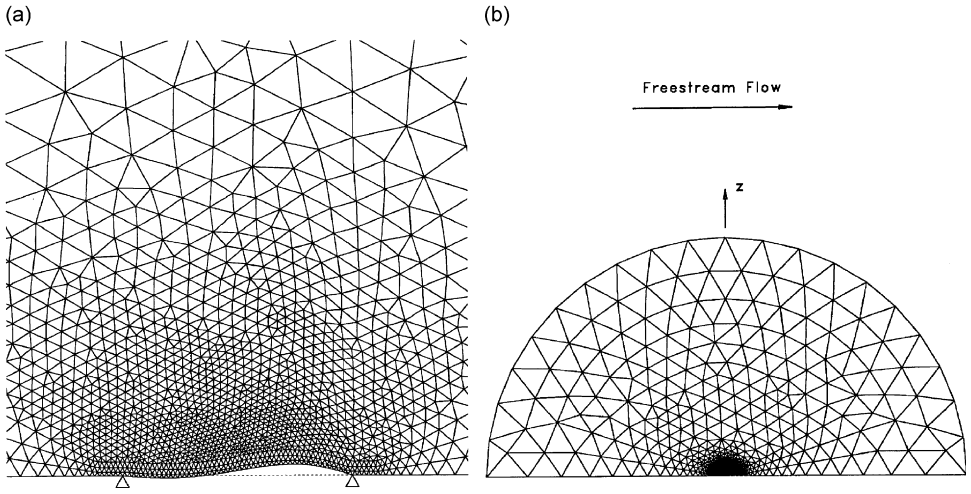

Fig. 5. Triangular unstructured mesh used in fluid domain in the transonic panel calculations: (a) near field view, illustrating mesh deformations; (b) far-field view.

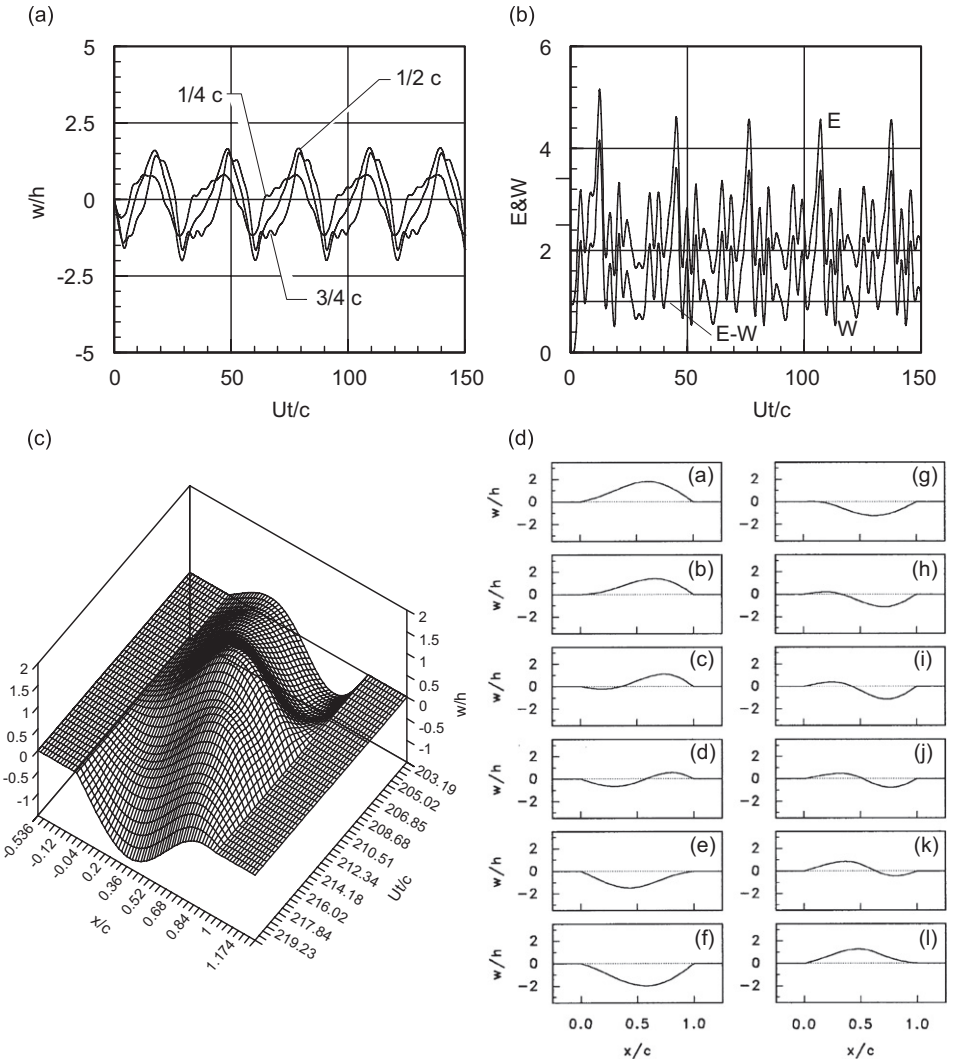

Fig. 6. Transonic travelling wave panel flutter at Mach 1. Simply supported aluminum panel at 20,000 ft, $h/c = 0.004$: (a) panel response at different chord locations; (b) panel total energy E and aerodynamic work W during flutter; (c) deflected shape of panel during flutter; (d) snap-shots of panel motion during one flutter period. In these and all subsequent panel figures, $U = U_\infty$.

travelling in the downstream direction. The limit cycle amplitude is essentially reached within one period of oscillation, suggesting a strong instability. The maximum amplitude w/h is around 1.5–2, which is within the range of validity of the von Kármán plate theory.

Although the motion is periodic, it is certainly not simple harmonic motion, nor is the wave form the same at all positions on the plate. The travelling wave may be considered a localized wave packet, which changes shape and "evolves" as it moves from the leading edge to the trailing edge of the panel. These interesting characteristics of the flutter mode arise from strong interactions between the nonlinearities in the fluid and the structure.

Fig. 6b shows the instantaneous energy history of the panel, which is periodic but highly irregular, with six peaks within each period. Here, E is the kinetic plus the strain energy, and W is the work done by the fluid on the entire panel. Fig. 6c shows the deflected shape of the panel during a typical half-period, illustrating the nonuniform downstream propagation of the flutter wave. Snapshots of the instantaneous panel deflections at equal time intervals during one complete LCO are presented in Fig. 6d. The flow next to the panel is mixed supersonic–subsonic, and supersonic pockets terminated by strong shocks exist next to the panel surface;

see Fig. 7. As the panel deflects, the shocks move in concert with the panel motion, sometimes vanishing over parts of the limit cycle period.

Inclusion of the geometric nonlinearities in the structural model is essential in order to obtain the correct stability behavior of the plate. If a linear structural model is used, no flutter is predicted in the transonic region near Mach 1-only panel divergence. Inclusion of the geometric nonlinearities completely changes the dynamic stability of the plate, and now travelling wave flutter is observed. It is interesting to note that in the transonic range between Mach 0.95 and 1.2, the structural and aerodynamic nonlinearities interact to generate travelling wave flutter even in panels of low chord-to-width ratio, where earlier studies based on linearized aerodynamics only predict single-degree-of-freedom flutter.

At transonic Mach numbers below unity, the prevailing panel instability is divergence, as discussed in Ref. [11]. Both outward and inward "aeroelastic buckling" of the panel occur, at least for cases where N_{x0} is zero. Strong shocks appear on the panel surface and are believed to play an important role in the divergence instability. If the nonlinear stiffening due to the in-plane load N_x is neglected (i.e., if a *linear* structural model is used), then a shock-induced, explosive divergence instability can occur over a range of transonic Mach numbers. In these cases, the panel deflections grow without bounds, until the aeroelastic code breaks down. These shock-induced divergence instabilities are often triggered after the panel displacements reach a critical amplitude during flutter, and have been observed (for the linear panel) at Mach numbers as high as 1.3.

For sufficiently thin panels, flutter becomes possible at transonic Mach numbers below unity. This is illustrated in Fig. 8a, for a simply supported aluminum panel with $h/c = 0.002$, at a Mach number of 0.95. As the Mach number at upstream infinity is increased through the range 1.0–1.3, the travelling wave character of the flutter mode, as indicated by temporal phase differences between the panel motions at the 1/4, 1/2, and 3/4 positions, gradually disappears. Around Mach 1.2, the strong shocks have also disappeared and the panel aeroelastic response becomes much more "regular", Fig. 8b. The flutter mode is now composed of a standing wave with a small travelling wave component superimposed, resulting in a mode that continually changes shape.

At higher Mach numbers, outside the transonic range, the flutter mode is again a standing wave. In the Mach number range 1.4–1.5, higher panel modes become excited, as reported in Ref. [11], but the modes are primarily of the standing wave type. These observations strongly suggest that the occurrence of travelling wave panel flutter in two-dimensional or high-aspect-ratio panels is a *transonic* phenomenon, brought about by the nonlinear aerodynamics. The presence of moving shocks on the panel surface becomes a strong driver in generating the complex flexural flutter waves observed in the panel. Structural nonlinearities appears to play a fundamental role as well, by coupling normal modes and by generating higher harmonics in the flutter wave that helps in generating travelling waves.

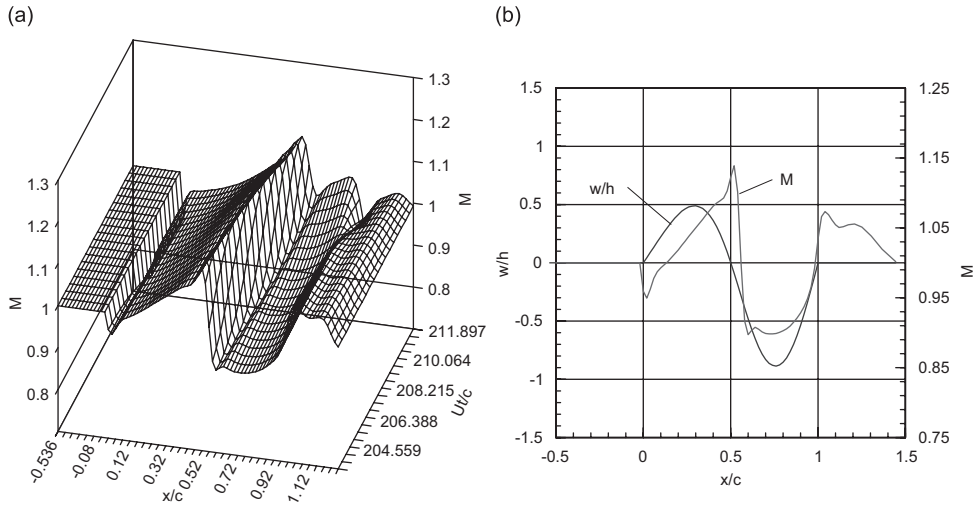

Fig. 7. (a) Mach number distribution at panel surface vs. time, (b) comparison with deflected panel shape.

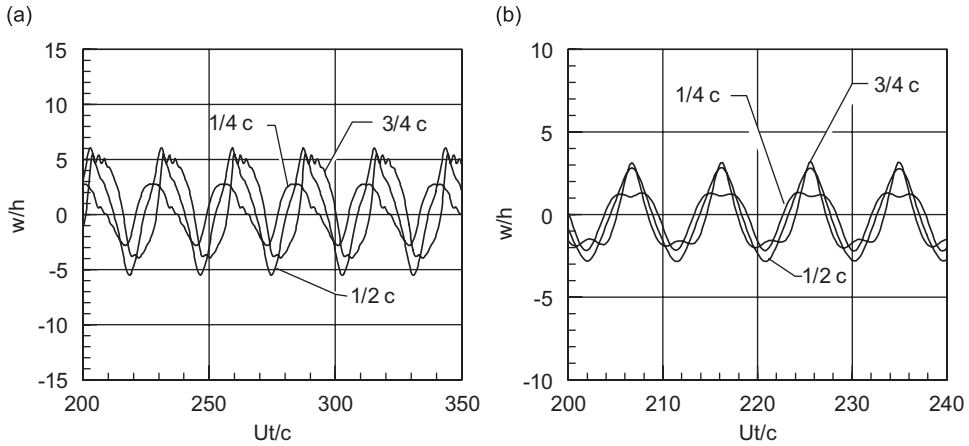

Fig. 8. Comparison of travelling wave flutter of panel at lower and upper ends of the transonic Mach number range: (a) Mach 0.95, $h/c = 0.002$, seal-level conditions; (b) Mach 1.2, $h/c = 0.004$, 20,000 ft altitude.

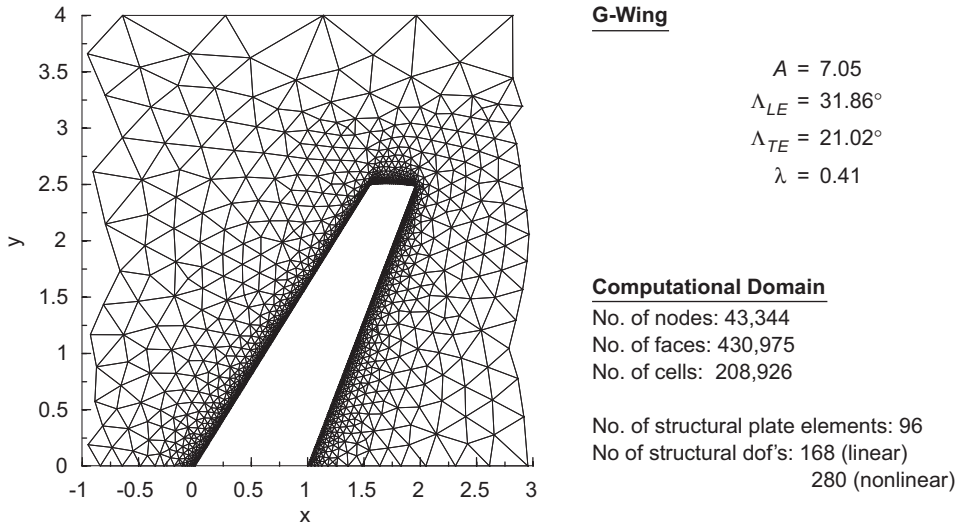

Fig. 9. The G-wing (generic transport wing) of similar planform to the wing studied experimentally in Ref. [7].

6.2. *Transonic limit cycle flutter of a high-aspect-ratio wing*

The G-wing shown in Fig. 9 is representative of high-aspect-ratio wings of modern transport aircraft, designed to cruise at high subsonic or transonic Mach numbers. It is similar to a wind tunnel model tested at DLR in Göttingen [7]. The effect of wing sweep is very pronounced, as it leads to strong interactions between structural (geometric) and aerodynamic nonlinearities, resulting in limit cycle flutter. If a linear structural model is used, no limit cycle flutter is predicted at the density and dynamic pressure where limit cycle flutter was observed in the wind tunnel tests, only stable decay to zero amplitudes, Fig. 10a. In order to trigger limit cycle flutter with the linear structural model, the dynamic pressure must be increased by 273%, Fig. 10b, but now the predicted flutter frequency is much higher (94 Hz) than was observed in the wind tunnel tests (50.4 Hz). The nonlinear structural model, on the other hand, predicts limit cycle flutter at the experimental Mach number and tunnel conditions reported in Ref. [7]; see Fig. 10c. The predicted flutter frequency of 52.4 Hz is very close (+4%) to the frequency of 50.4 Hz observed during wind tunnel tests. The Direct Eulerian–Lagrangian computational method was used in all of the swept wing calculations, using the Mindlin–Reissner finite element model outlined in Section 3.2.

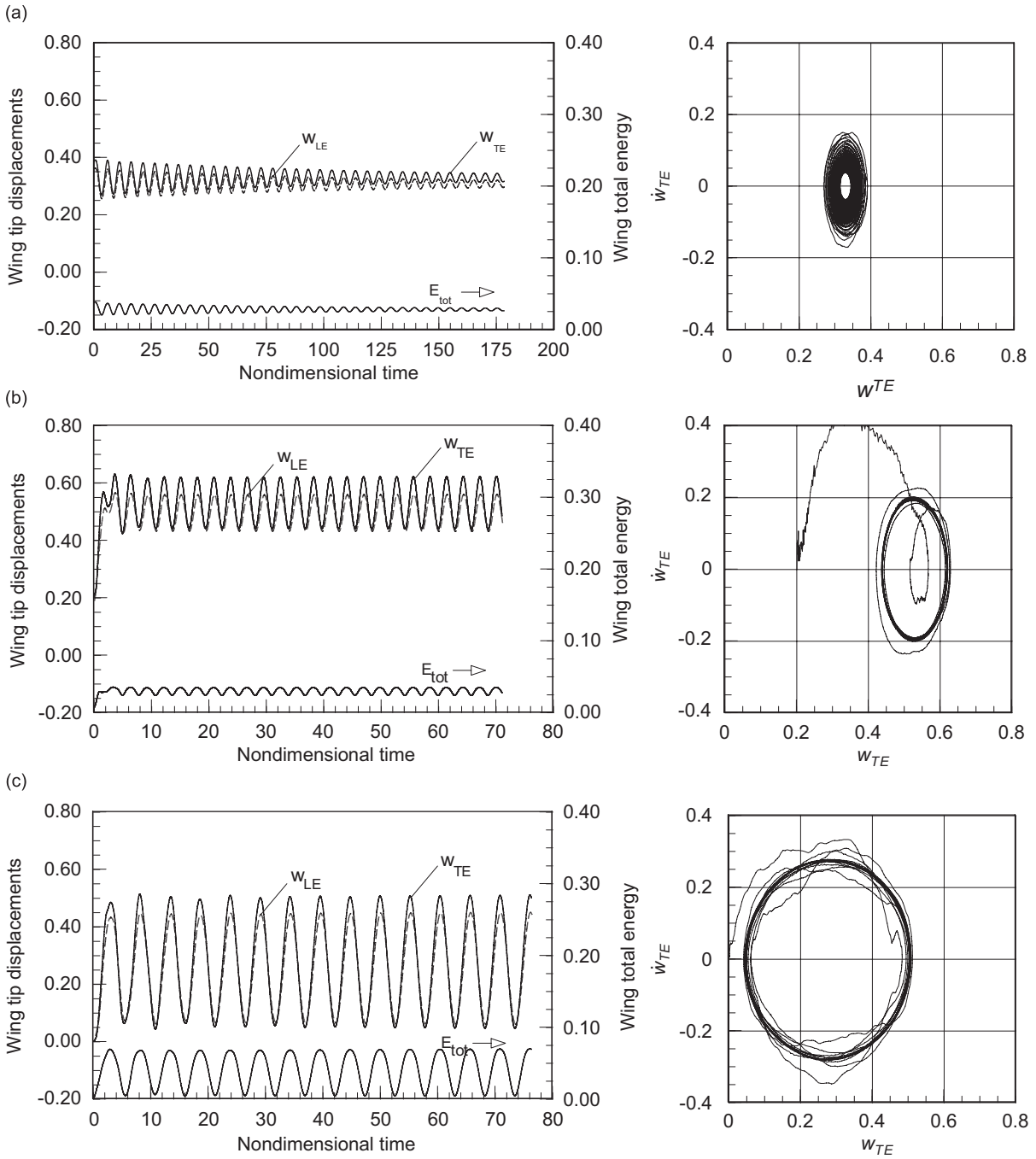

Fig. 10. Comparison of limit cycle flutter prediction using linear vs. nonlinear structural models: (a) linear structure and $\rho_a = 0.4177\,\mathrm{kg/m^3}$; (b) linear structure and $\rho_a = 1.141\,\mathrm{kg/m^3}$; (c) nonlinear structure and $\rho_a = 0.4177\,\mathrm{kg/m^3}$.

The reason for the large differences between the LCO amplitudes predicted using the linear vs. the nonlinear Mindlin–Reissner FE models can be understood in terms of the effect that the structural washout phenomenon has on the transonic flow-field around the wing, especially on the location and motion of the part-chord shocks on the wing surface. The structural washout effect is illustrated in Fig. 11, and arises from the fact that streamwise wing segments undergo different rotations about the unswept y-axis than do chordwise segments. In the case of a high-aspect-ratio swept wing, the structural washout effect from

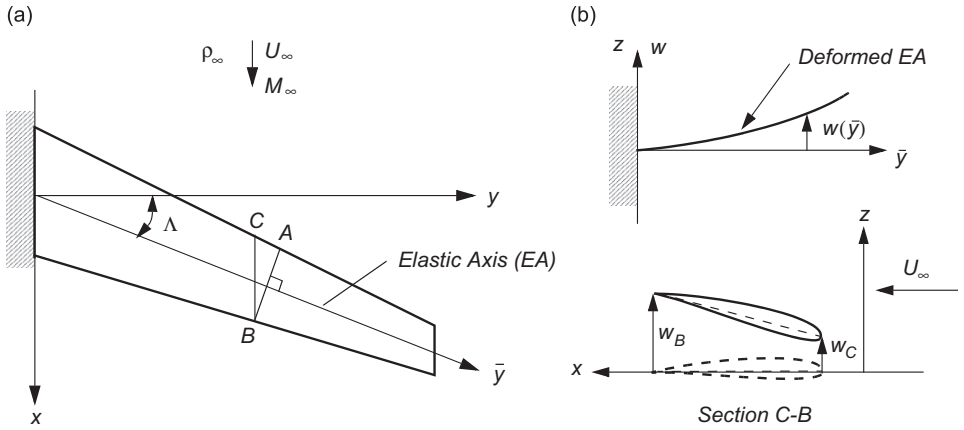

Fig. 11. (a) Chordwise segment $A–B$ vs. streamwise segment $C–B$ of a swept wing; (b) structural washout effect (reduction of angle of attack of streamwise segment $C–B$, since $w_C < w_B$).

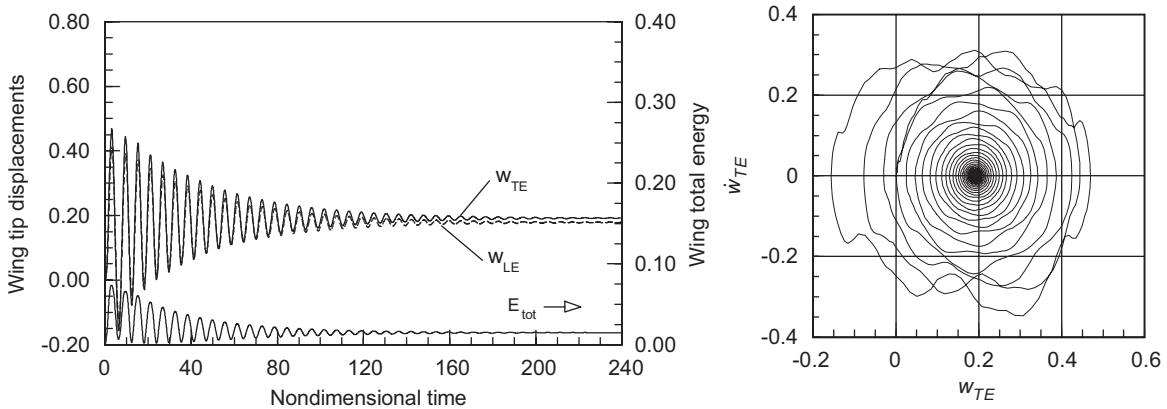

Fig. 12. Stable decay of the G-Wing tip amplitudes at Mach 0.75.

aeroelastic deformations plays a fundamental role in throttling the energy flow from the airstream to the wing, resulting in limit cycle flutter. As the wing bends, the washout reduces the angle of attack of streamwise chord sections, unloading the outboard region of the wing, reducing the shock strength and shifting the part-chord shocks in the upstream direction. The weaker and more forward shocks lead to an earlier transition (at lower amplitudes) from Type A to Type B shock motion, which decreases the aerodynamic work by the air on the wing, per cycle, resulting in a limit cycle flutter.

Although the nonlinear structure is stiffer than the corresponding linear structure, it is actually less stable for this class of wings, because the structural washout is also less. The aeroelastic problem is inherently nonlinear, and neither the aerodynamic nor the structural nonlinearities can be ignored, or an incorrect assessment of aeroelastic stability is obtained. The strong interactions between aerodynamic and structural nonlinearities lead to an interesting limit cycle flutter behavior of the G-wing, where limit cycle flutter is observed over a wide range of transonic Mach numbers, air densities (or altitudes), and dynamic pressures. In some cases, the calculated limit cycle flutter amplitudes were observed to increase with decreasing air density, suggesting that high-altitude transonic flutter might occur, even if the wing is stable at lower altitudes.

No instances of LCO-type flutter were detected at subcritical Mach numbers. Fig. 12 shows the calculated aeroelastic response for Mach 0.75. It is believed that the flow around the wing is entirely subsonic in this case, and the dynamic response shows exponential decay. Fig. 13 shows the predicted LCO flutter amplitude vs. Mach number, for an air density of 0.4177 kg/m^3, which corresponds to a density altitude of roughly 10 km (32,800 ft). Except in the Mach number range 0.89–0.96, the LCO amplitudes are stable, although subtle

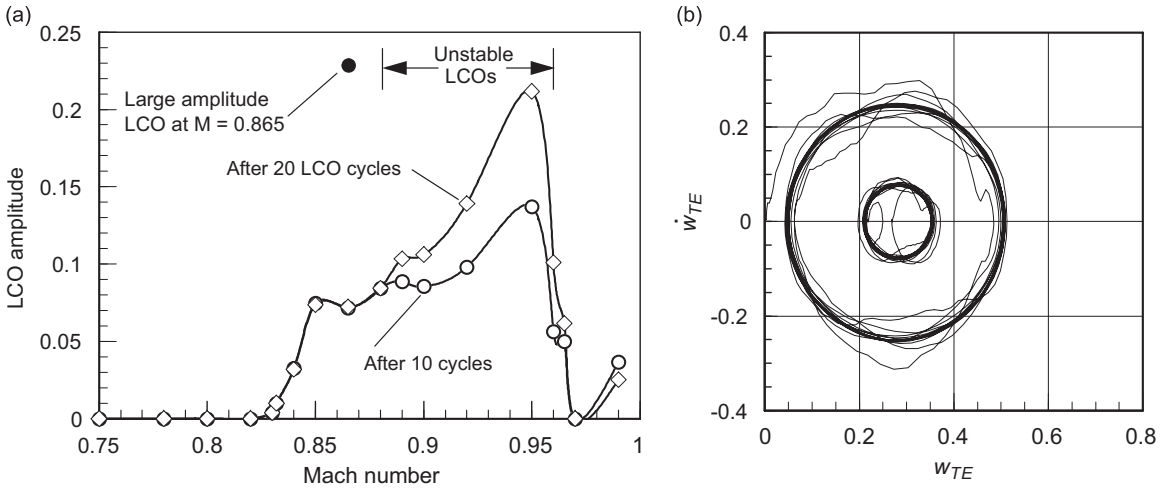

Fig. 13. (a) Limit cycle flutter amplitude vs. Mach number at a constant air density of $\rho_a = 0.4177\,\mathrm{kg/m^3}$, corresponding to a density altitude of approximately 32,800 ft (10,000 m); (b) nested LCOs of different amplitudes at Mach 0.865, depending on initial conditions. Sea-level standard day temperature.

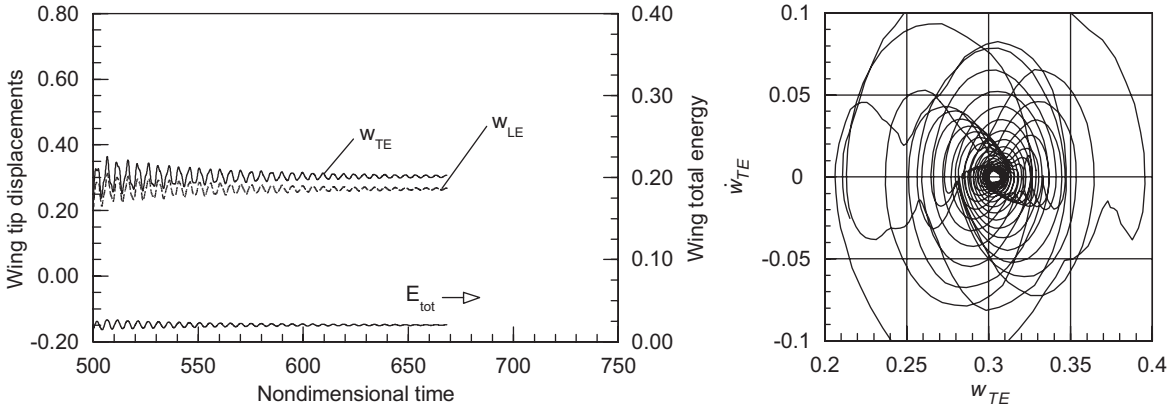

Fig. 14. Stable decay of the G-wing at Mach 0.97.

"nonclassical" behaviors are observed; that is, the motion does not appear exactly periodic, nor does it appear to converge to such a state even after many oscillation cycles. This is reflected in the phase plots as a "smearing" or "broadening" of the limit cycle, and is believed to be caused by irreversible (nonconservative) interactions between the structural nonlinearities arising from large deflections, and aerodynamic nonlinearities caused by moving shocks (entropy production).

In the Mach number range 0.89–0.96, the limit cycle flutter mode exhibits an amplitude instability, reflected by a slowly growing LCO amplitude starting at Mach 0.89, with a progressively increasing growth rate as the Mach number is increased. This instability is believed to be triggered by a weak nonuniformity on the time scale, which causes the basin of attraction of the limit cycle to change with time. It is a reminder that we a dealing with an essentially *nonconservative* nonlinear system, and classical concepts from nonlinear dynamics based on potential theory may not apply. At Mach 0.865, two stable limit cycles were observed, depending on the initial conditions, Fig. 13b. It is likely that such nested LCOs extend to other neighboring Mach numbers as well.

Between Mach 0.96 and 0.97, the LCO amplitudes undergo a rapid decay to zero, as shown in Fig. 14. At Mach 0.99, at limit cycle of very small amplitude reappears (not shown). The reason for this surprising behavior is not fully understood, but is believed to be closely connected with the progressive aft movement of

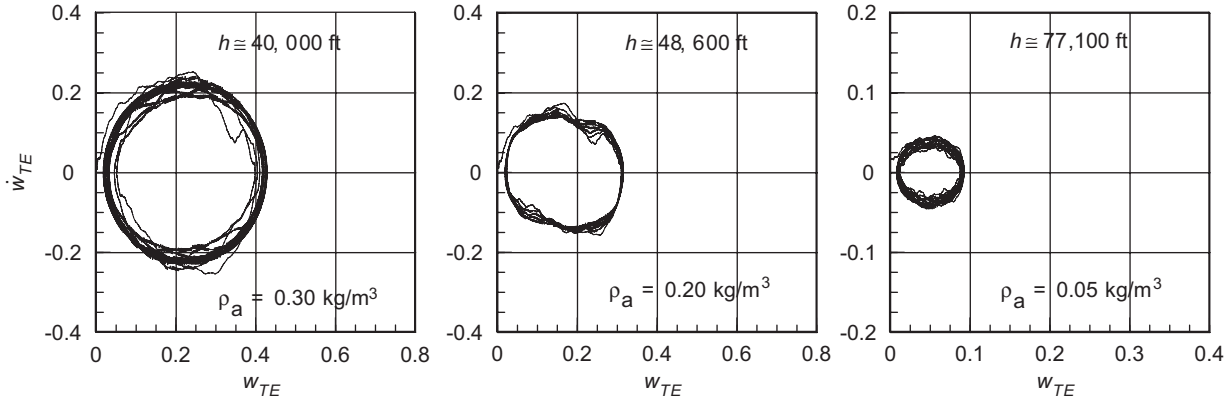

Fig. 15. Phase plots of LCO flutter at high altitudes ($M_\infty = 0.865$; temperature effects neglected).

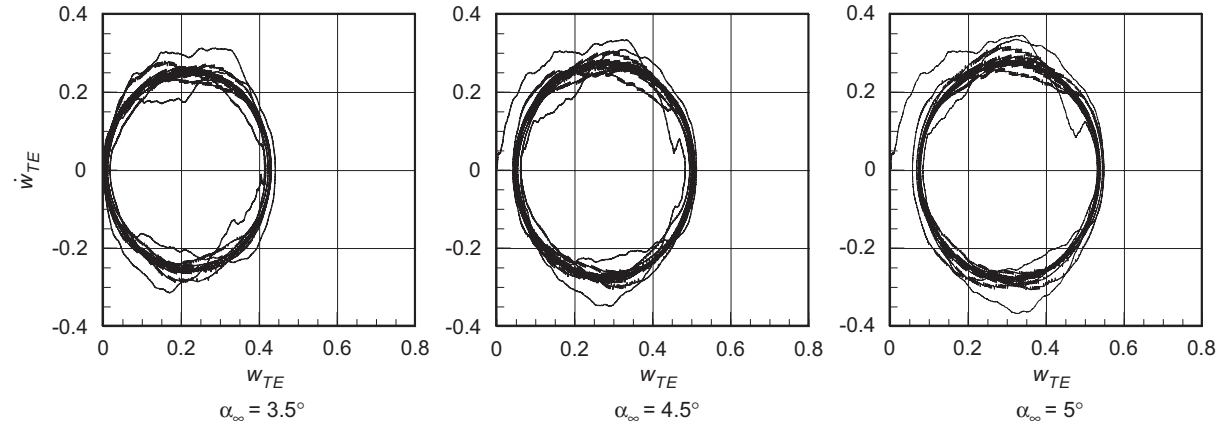

Fig. 16. Effect of angle of attack on limit cycle flutter (LCO) amplitude of the G-wing at Mach 0.865 and air density $\rho_a = 0.4177\,\mathrm{kg/m^3}$, as predicted by the fully nonlinear aeroelastic model.

the mean positions of the part-chord shocks, and the fact that the shocks approach the trailing edge as $M_\infty \to 1$. It should be noted that the temperature has been kept constant at the sea level, standard day value of 59 °F (518.7 °R or 288.15 K) in these calculations. This would correspond to wind tunnel tests were the density and Mach number are varied while keeping the air temperature roughly constant at ambient conditions.

Because of strong interactions between the structural and aerodynamic nonlinearities, limit cycle flutter is predicted over a wide range of altitudes (or air densities/dynamic pressures). At Mach 0.865, for example, the LCO-type flutter of the G-wing persists down to very low densities, representing density altitudes well into the stratosphere, as shown in Fig. 15. In some cases, the calculated limit cycle flutter amplitudes were observed to increase with decreasing air density, suggesting that high-altitude transonic flutter could become an issue.

Finally, Figs. 16 and 17 illustrate the relative insensitivity of the LCO amplitudes to angle of attack, for two different air densities (or altitudes). These results suggest that the limit cycle flutter behavior for this particular wing is not isolated, but persists over a wide range of flight altitudes and aircraft trim conditions.

6.3. Comparison of structural and computational models

As mentioned in the Introduction, the von Kármán structural model does not perform well in aeroelastic stability problems involving cantilevered wings in general, not just high-aspect-ratio wings. Fig. 18 shows a comparison of the calculated flutter behavior of the ONERA M6 wing at Mach 0.84, as obtained using the von Kármán structural model and compared to the results obtained with the linear and fully nonlinear models

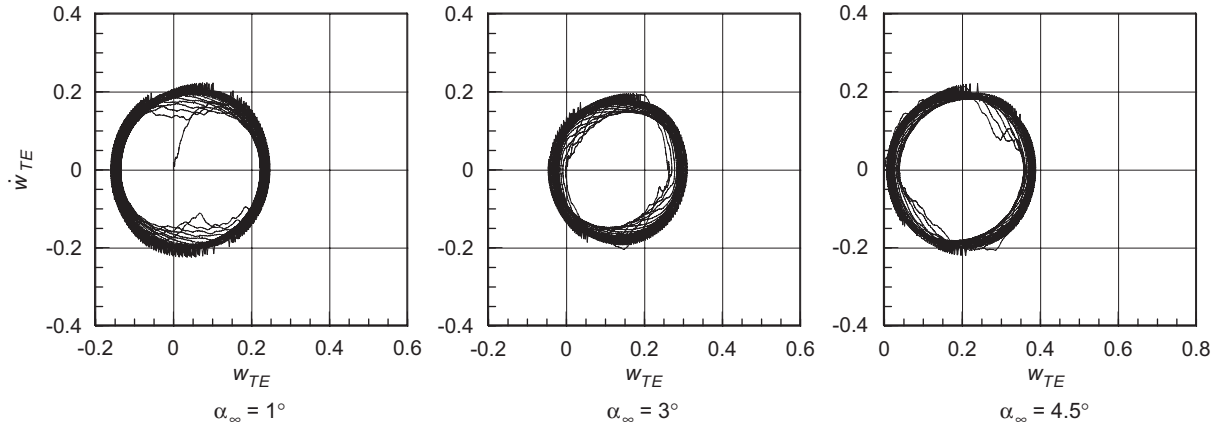

Fig. 17. Effect of angle of attack on limit cycle flutter (LCO) amplitude of the G-wing at Mach 0.865 and air density $\rho_a = 0.25\,\mathrm{kg/m^3}$, as predicted by the fully nonlinear aeroelastic model.

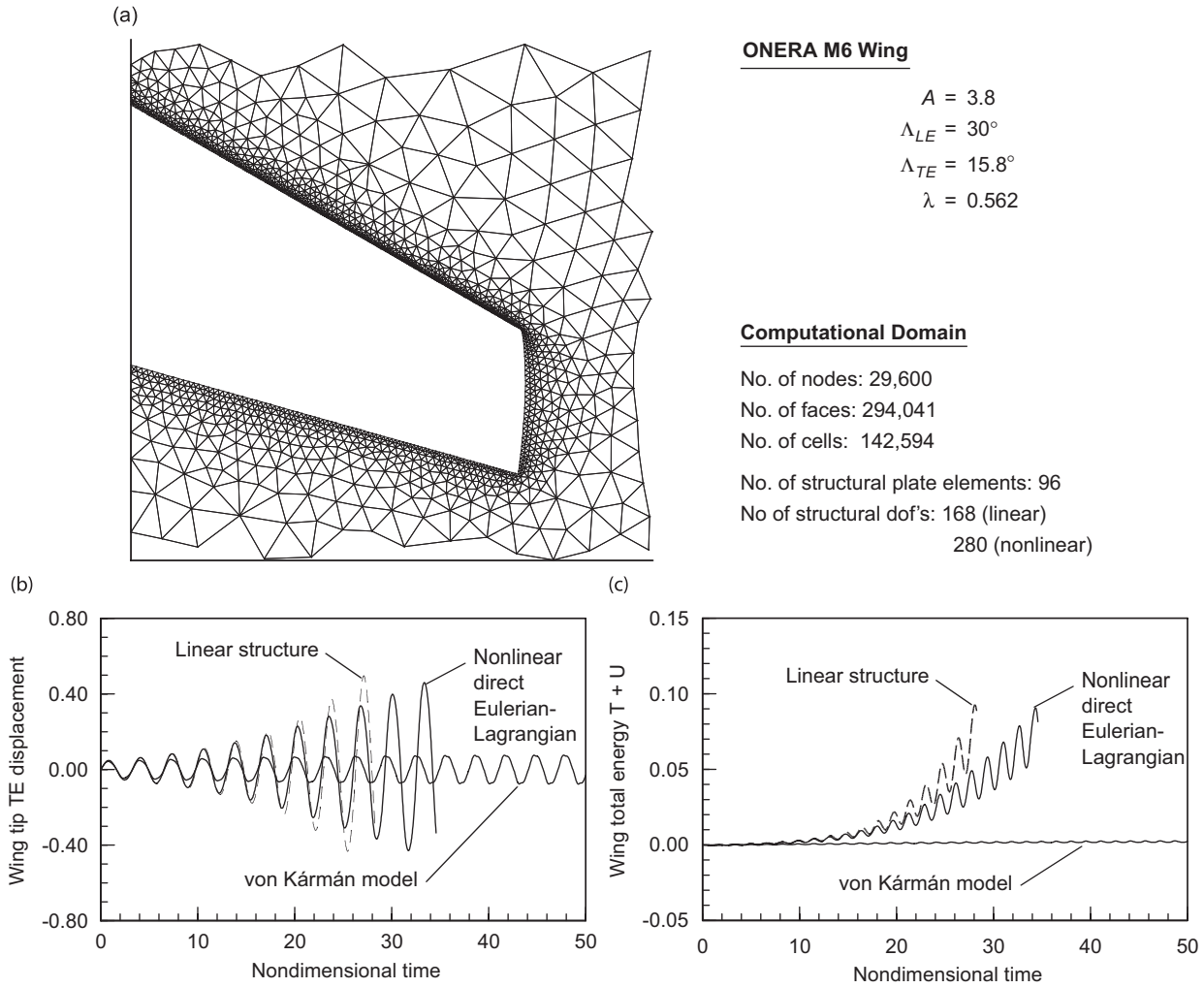

Fig. 18. Comparison of the predicted aeroelastic response of the ONERA M6 wing model, using different structural models.

discussed in Section 3 of this paper. This wing is of moderate aspect ratio ($A = 3.8$) and calculations based on a linear structural model have been presented in Ref. [9]. As can be seen from Fig. 18, the aeroelastic calculation based on the von Kármán model greatly underestimates the growth of the wing total energy, Fig. 18b, and thus completely misses the explosive nature of the emerging flutter. In fact, the *linear* structural model does a better job, both qualitatively and quantitatively, in this example.

7. Concluding remarks

In both example problems considered in this paper, the combined effect of structural and aerodynamic nonlinearities on the stability of the fluid–structure system is much larger and qualitatively different than what would be anticipated from the individual effects of the structural and fluid nonlinearities, if considered separately. If a linear structural model is used with nonlinear Euler-based aerodynamics in the panel case, for example, only nonphysical divergence instabilities are observed in the transonic region. Similarly, in the case of the high-aspect-ratio wing considered in Section 6, if a linear structural model is used with nonlinear aerodynamics, the calculated transonic flutter dynamic pressure is higher than the experimental value by almost a factor of 3, and the predicted limit cycle flutter frequency is much higher than was observed during wind tunnel tests.

For plates where all edges are fixed or simply supported, the von Kármán model performs reasonably well, although it overestimates the stiffness of the structure and thus tends to underestimate the limit cycle flutter amplitudes. But in the case of cantilevered wings undergoing moderate to large deflections, it greatly overestimates the stiffening effects arising from the in-plane strains, leading to a significant underestimation of the limit cycle flutter amplitudes, or to an erroneous prediction of no flutter, as in the case of the case of the high-aspect-ratio transonic wing considered in this study.

In the high-aspect-ratio swept wing example, the structural washout effect from aeroelastic deformations plays an important role in determining flutter stability, resulting in a strong coupling between the geometric structural nonlinearities and the aerodynamic nonlinearities caused by shock motion. For swept wings of sufficient flexibility, the aeroelastic washout effect can produce the counterintuitive result that *decreasing* the dynamic pressure by decreasing the density at a given Mach number may actually be destabilizing—a conclusion of obvious practical relevance to both wind tunnel and flight testing.

Acknowledgments

This research was supported by NASA Grants NCC 2-374 and NCC 4-157, and NASA Contract NND05AD23P.

References

[1] E.H. Dowell, Nonlinear oscillations of a fluttering plate, *AIAA Journal* 4 (1966) 1267–1275.
[2] C. Mei, A finite element approach for nonlinear panel flutter, *AIAA Journal* 15 (1977) 1107–1110.
[3] M.J. Patil, D.H. Hodges, C.E.S. Cesnik, Nonlinear aeroelasticity and flight dynamics of high-altitude long endurance aircraft, *Journal of Aircraft* 38 (1) (2001) 88–94.
[4] D. Tang, J. Henry, E. Dowell, Limit cycle oscillations of delta wing models in low subsonic flow, *AIAA Journal* 37 (1999) 155–164.
[5] P.J. Attar, E.H. Dowell, J.R. White, Modeling delta wing limit-cycle oscillations using a high-fidelity structural model, *AIAA Journal of Aircraft* 42 (2005) 1209–1217.
[6] G. Schewe, A. Knipfer, H. Mai, G. Dietz, Nonlinear effects in transonic flutter, *International Forum on Structural Dynamics and Aeroelasticity 2001*, Madrid, Spain, June 2001.
[7] G. Dietz, G. Schewe, F. Kiessling, M. Sinapius, Limit-cycle-oscillations of a transport aircraft wing model, *Proceedings of the International Forum on Structural Dynamics and Aeroelasticity 2003*, Amsterdam, The Netherlands, June 4–6, 2003.
[8] O.O. Bendiksen, Transonic limit cycle flutter/LCO, AIAA Paper 2004-1694, *Proceedings of the AIAA/ASME/ASCE/AHS/ASCE 45th SDM Conference*, Palm Springs, CA, April 19–22, 2004.
[9] O.O. Bendiksen, Modern developments in computational aeroelasticity, *Journal of Aerospace Engineering, Proceedings of the Institution of Mechanical Engineers* 218 (Part G) (2004) 157–177.
[10] G. Seber, O.O. Bendiksen, Nonlinear flutter calculations using finite elements in a large deformation direct Eulerian–Lagrangian formulation, AIAA Paper 2005-1856, *Proceedings of the 46th AIAA/ASME/ASCE/AHS/ASC Structures, Structural Dynamics, and Materials Conference*, Austin, TX, April 18–21, 2005.

[11] G.A. Davis, O.O. Bendiksen, Transonic panel flutter, AIAA Paper 93-1476, April 1993.
[12] O.O. Bendiksen, G.A. Davis, Nonlinear travelling wave flutter in panels in transonic flow, AIAA Paper 95-1496, *AIAA/ASME/ASCE/AHS/ASC 36th Structures, Structural Dynamics, and Materials Conference*, New Orleans, LA, April 10–12, 1995.
[13] R.E. Gordnier, Computation of limit cycle oscillations of a delta wing, AIAA Paper 2002-1411, *Proceedings AIAA/ASME/ASCE/AHS/ASCE 43rd SDM Conference*, Denver, CO, April 22–25, 2002.
[14] H.C. Nelson, H.J. Cunningham, Theoretical investigation of flutter of two-dimensional flat panels with one surface exposed to supersonic potential flow, NACA Report 1280, 1956.
[15] H.J. Cunningham, Flutter analysis of flat rectangular panels based on three-dimensional supersonic unsteady potential flow, NASA TR R-256, 1967.
[16] E.H. Dowell, Nonlinear oscillations of a fluttering plate, *AIAA Journal* 4 (1966) 1267–1275.
[17] E.H. Dowell, Theoretical–experimental correlation of plate flutter boundaries at low supersonic speeds, *AIAA Journal* 6 (1968) 1810–1811.
[18] J. Dugundji, E. Dowell, B. Perkin, Subsonic flutter of panels on continuous elastic foundations, *AIAA Journal* 1 (1963) 1146–1154.
[19] J.G. Eiseley, The flutter of a two-dimensional buckled plate with clamped edges in supersonic flow, California Institute of Technology, AFOSR TN 56-296, 1956.
[20] Y.C. Fung, Some recent contributions to panel flutter research, *AIAA Journal* 1 (1963) 898–909.
[21] J.L. Batoz, P. Lardeur, A discrete shear triangular nine D.O.F. element for analysis of thick to very thin plates, *International Journal for Numerical Methods in Engineering* 28 (1989) 533–560.
[22] G. Hwang, Parallel Finite Element Solutions of Nonlinear Aeroelastic and Aeroservoelastic Problems in Three-Dimensional Transonic Flows, PhD Dissertation, Mechanical and Aerospace Engineering Department, University of California, Los Angeles, CA, March 1997.